Thermomechanical analysis of the tensile test: simulation and experimental validation

Diego J. Celentano[†]

Departamento de Ingeniería Mecánica, Universidad de Santiago de Chile,
Av. Bdo. O´Higgins 3363, Santiago, Chile

Abstract.   This paper presents experimental and numerical analyses of the thermomechanical behaviour that takes place in SAE1020 mild steel cylindrical specimens during the conventional tensile test. A set of experiments has been carried out in order to obtain the stress-strain curve and the diameter evolution at the neck which allow, in turn, to derive the elastic and hardening parameters characterizing the material response. Temperature evolutions have also been measured for a high strain rate situation. Moreover, a finite element large strain thermoelastoplasticity-based formulation is proposed and used to simulate the deformation process during the whole test. Some important aspects of this formulation are discussed. Finally, the results provided by the simulation are experimentally validated.

Key words: tensile test; coupled thermomechanical problems; large strains; thermoplasticity; finite element formulations.

1. Introduction

The tensile test is an important standard engineering procedure useful to characterize some relevant elastic and plastic variables related to the mechanical behaviour of materials. Due to the non-uniform stress and strain distributions existing at the neck for high levels of axial deformation, it has been long recognized that significant changes in the geometric configuration of the specimen have to be considered in order to properly describe the material response during the whole deformation process up to the fracture stage.

The necking process of a bar used in the tensile test has been extensively studied by means of analytical expressions for the stress distribution at the neck based on some geometric considerations of the deformation pattern (see e.g., Nádai 1950 and Bridgman 1952). In recent years, several finite element large strain formulations usually defined within the plasticity framework have been developed and applied to the analysis of this test under isothermal and non-isothermal conditions (see e.g., Simo and Armero 1992, García Garino and Oliver 1993, Simo 1995, Goicolea *et al.* 1996 and references therein for the first case and Wriggers *et al.* 1989, Armero and Simo 1993 for the second one). In this latter case, the influence of different effects on the thermomechanical response have been particularly analysed, such as the adiabatic limiting situation and the consideration of temperature-dependent hardening laws. Moreover, some of such formulations have been validated,

---

† Professor

mainly under isothermal conditions, with experimental data considering different materials.

The aim of this paper is to present an experimental analysis and a numerical simulation of the thermomechanical behaviour of SAE1020 mild steel cylindrical specimens subjected to the tensile test. The experimental procedure undertaken to characterize some specific features of the material response is described in Section 2. To this end, two different load cell speeds have been considered in order to achieve nearly isothermal and non-isothermal conditions. In particular, the derivation of the parameters involved in the assumed exponential plastic hardening law together with the data acquisition of temperature caused by plastic deformation are also detailed. Moreover, the coupled thermomechanical formulation proposed to simulate the deformation process that takes place during the test is presented in Section 3. This large strain isotropic thermoelastoplasticity-based formulation includes the definitions of a specific free energy function and plastic evolution equations which are the basis to derive all the material constitutive relations. The corresponding finite element model is briefly presented in Section 4 where two important original aspects are discussed: the solution of the resulting system of equations via an improved staggered scheme and a particular treatment of the incompressible plastic flow in order to overcome the well-known volumetric locking in the numerical behaviour. It should be mentioned that this finite element formulation is an alternative approach to existing methodologies dealing with large plastic deformations.

The numerical simulation of the tensile test applied to cylindrical specimens is performed in Section 5. The behaviour of the HE30 (BS 1474) aluminium alloy is firstly studied under isothermal conditions since previously published experimental and numerical results useful for comparison are available for this case (see Goicolea *et al.* 1996). Later, as mentioned above, the results obtained with the proposed formulation considering SAE1020 steel specimens are validated with the corresponding experimental measurements. Different results at the section undergoing extreme necking are specifically analysed: ratio of current to initial diameter in terms of the elongation and both load and mean true axial stress versus logarithmic strain. Furthermore, the validation task comprises the analysis of temperature evolutions at three locations of the specimen. Although the mechanical behaviour is not mainly affected by the temperature levels that can be obtained in conventional tension machines due to the relatively low strain rates experienced by the specimen (usually the maximum load cell is about 500 mm/min), the prediction of the generated plastic work is an important feature in order to estimate temperature evolutions which definitely play a major role in other material tests (e.g., the Taylor impact test) in which the thermal softening effect can not be neglected (Zerilli and Armstrong 1987). Finally, a numerical assessment of the performance of different discretizations and element topologies is also illustrated.

2. Experimental procedure

The experimental procedure adopted in this work to characterize the mechanical behaviour of a material consisted in the following steps:

1) Selection of the material and the specimens to be tested according to the ASTM standards (Annual Book of ASTM Standards 1988). The chosen SAE1020 mild steel cylindrical specimen with a nominal diameter of 9 mm is sketched in Fig. 1. The distance between the two black markers denotes the initial extensometer length taken as 50 mm. A nearly linear gradual reduction in diameter is considered in order to trigger the necking development which has to take place approximately at the middle of the extensometer length. This tapered profile fits the ASTM
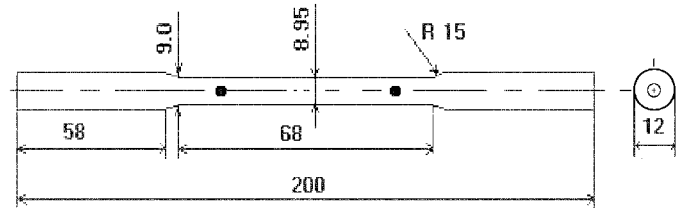
Fig. 1 Analysis of a SAE1020 steel cylindrical tension specimen: geometry

Table 1 Analysis of a SAE1020 steel cylindrical tension specimen: average chemical composition (% in weight)

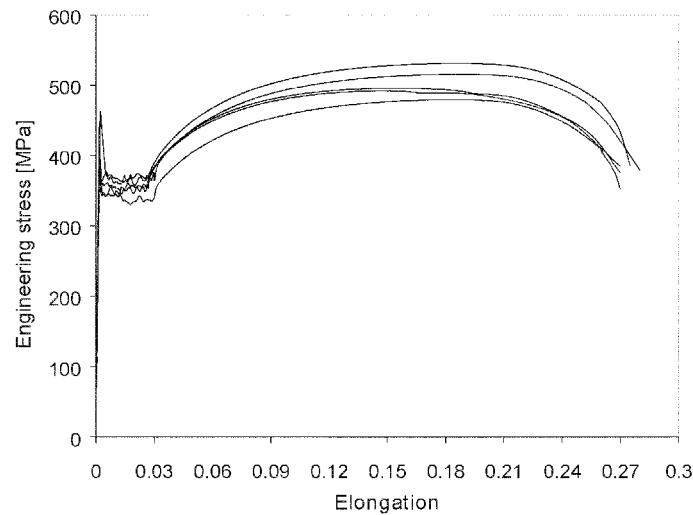| %C	%Si	%Mn	%P	%S
0.202	0.151	0.557	0.0155	0.0627
%Cr	%Mo	%Ni	%Al	%Cu
0.113	0.0282	0.102	0.0252	0.240
%Nb	%Ti	%V	%W	%Pb
0.0052	0.00321	0.00571	0.0224	<0.005
%Sn	%B	%Fe	%Co	
0.0242	0.00038	98.43	0.0215	

Fig. 2 Analysis of a SAE1020 steel cylindrical tension specimen: experimental stress-strain curves obtained with five specimens considering a load cell speed of 2.5 mm/min leading to nearly isothermal conditions

standards since the difference between the maximum and minimum diameter values (9 mm and 8.95 mm, respectively) existing in the extensometer length is lower than 1%.

2) Chemical characterization to check an adequate composition according to the selected material.

Table 2 Analysis of a SAE1020 steel cylindrical tension specimen: average
experimentally measured material properties

Young's modulus	222054 MPa
Yield strength (elongation: 0.2%)	333.0 MPa
Hardening coefficient	730.75 MPa
Hardening exponent	0.1845
Maximum engineering stress	470 MPa
Elongation at the maximum load	18.5%
Elongation at the fracture stage	27.2%

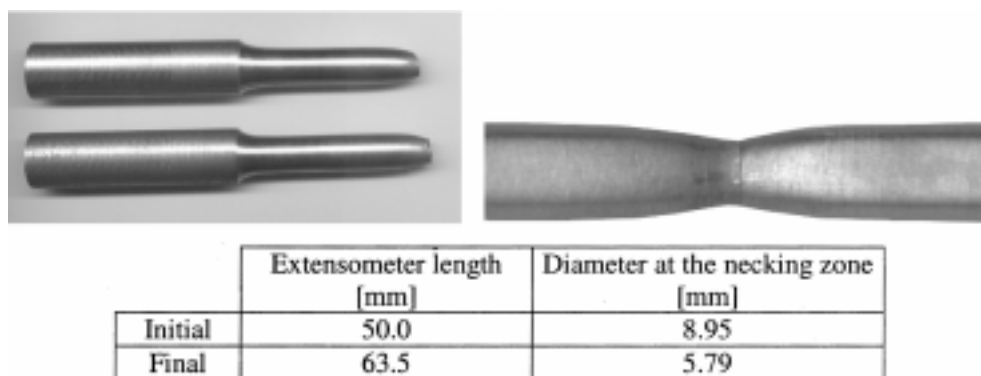|	Extensometer length [mm]	Diameter at the necking zone [mm]
Initial	50.0	8.95
Final	63.5	5.79

Fig. 3 Analysis of a SAE1020 steel cylindrical tension specimen: geometric configuration at the end of the test

This routine task is carried out by means of an optical spectrometer. The average chemical composition is shown in Table 1 where, in particular, the carbon content agrees with the specified value corresponding to SAE1020 steel.

3) Mechanical tensile testing. The stress-strain curves obtained with five specimens considering a load cell speed of 2.5 mm/min are plotted in Fig. 2. As usual, the engineering stress is defined as P/A_0, where P is the axial load and A_0 is the initial transversal area with diameter D_0 while the engineering strain or elongation is computed as $(L - L_0)/L_0$, with L and L_0 being the current and initial extensometer lengths, respectively. The appearance of plastic deformation without hardening up to an elongation of 4% is a typical phenomenon observed in low carbon steels known as Lüders-band formation (Dieter 1988). From this point onwards, the hardening begins and the load increases reaching a maximum value for an elongation of approximately 18%. Then, the load decreases since the effect of the reduction of the transversal area at the necking zone is stronger than that of the hardening mechanism. The average measured values for the Young's modulus E, yield strength, maximum engineering stress and elongations at the maximum load and at the fracture stage are summarized in Table 2. The geometric configuration of a broken specimen at the end of the test is shown in Fig. 3.

Table 3 Analysis of a SAE1020 steel cylindrical tension specimen: correction factor for the stress distribution at the neck (see Bridgman 1952)

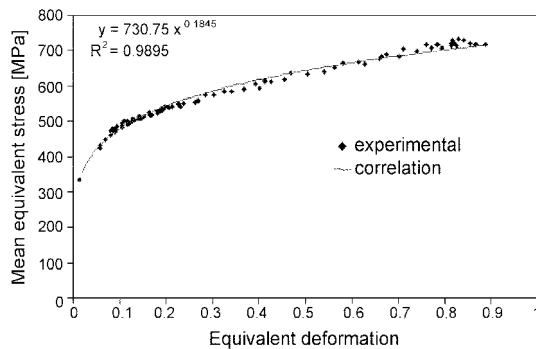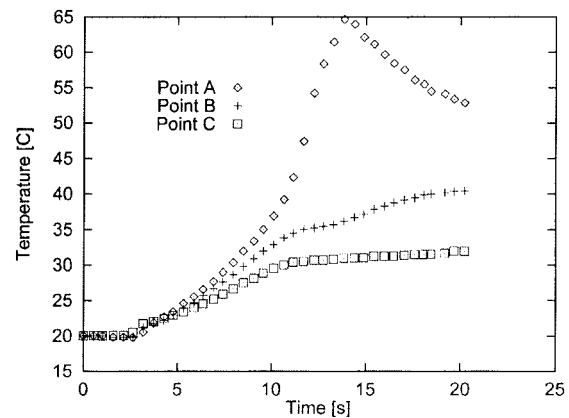| Correction factor f_B	$\ln(A_0/A)$
1.000	0.0
1.000	0.1
0.978	0.2
0.957	0.3
0.938	0.4
0.921	0.5
0.905	0.6
0.890	0.7
0.876	0.8
0.863	0.9
0.851	1.0

Fig. 4 Analysis of a SAE1020 steel cylindrical tension specimen: mean equivalent stress versus equivalent deformation obtained with four specimens considering a load cell speed of 2.5 mm/min leading to nearly isothermal conditions

Point positions at the initial configuration	A	B	C
Radial direction [mm]	4.5	4.5	4.5
Axial direction [mm]	5.0	15.0	25.0

Fig. 5 Analysis of a SAE1020 steel cylindrical tension specimen: experimental temperature evolutions considering a load cell speed of 100 mm/min leading to non-isothermal conditions

4) Characterization of the plastic behaviour. At high levels of elongation, the stress and strain distributions are no longer uniform along the specimen due to the necking formation. Therefore, the stress-strain curve of Fig. 2 can not provide a proper description of the physical phenomena involved in the test. Following the procedure proposed by Bridgman (1952), the mechanical response can be adequately described by an alternative stress-strain curve defined in terms of the

mean equivalent stress $\overline{\sigma}_{eq}$ versus an equivalent deformation ε_{eq} (composed of an elastic and plastic contributions) respectively given by $\overline{\sigma}_{eq} = f_B P/A$ and $\varepsilon_{eq} = \overline{\sigma}_{eq}/E + \varepsilon_p$, where $f_B(\varepsilon_p) \leq 1$ is a known correction factor applied to the mean true axial stress P/A (see Table 3), A is the current transversal area at the necking zone, $\varepsilon_p = \ln(A_0/A) = -2\ln(D/D_0)$ is the logarithmic deformation and D is the current diameter of the neck. As can be seen, D is the additional variable to be measured in order to obtain such stress-strain relationship. Fig. 4 shows the $\overline{\sigma}_{eq} - \varepsilon_{eq}$ experimental data for four specimens and the exponential correlation derived from them. It should be noted that the two constants involved in this correlation (see also Table 2) are assumed to define the material hardening behaviour described by an isotropic strain hardening law shown in the next Section.

5) Characterization of the thermal response caused by plastic deformation. A portion of the mechanical work needed to deform the specimen is transformed into a heat source which promotes a rise of temperature mainly at the neck. This effect was almost negligible for the load cell velocity mentioned above and, therefore, higher strain rates are needed to be able to observe some significant heating. The experimental temperature evolutions at three different (J type) thermocouple locations considering a load cell speed of 100 mm/min with an initial (laboratory) temperature of 20ºC are presented in Fig. 5. The temperature distribution is not uniform along the specimen where, as expected, larger values are found for points situated at smaller distances to the neck. The fracture of the specimen occurs at 12 s approximately. The curve corresponding to point A clearly shows that the time delay in the thermocouple measurements is about 2 s since the temperature reaches a maximum value at 14 s when the specimen is already broken. Finally, it is important to remark that no rate-dependency was observed in this material under the isothermal and non-isothermal conditions (i.e., at low and high cell load speeds, respectively) tested in this work since the corresponding stress-strain curves were practically the same for both situations.

The curves and parameters obtained in this experimental procedure are the basic data for the numerical simulation and experimental validation presented in Section 5.

3. Thermomechanical formulation

In a general thermomechanical context, the local governing equations describing the evolution of a process can be expressed by the continuity equation, the equation of motion, the energy balance and the dissipation inequality (all of them valid in $\Omega x\Upsilon$, where Ω is the spatial configuration of a body and Υ denotes the time interval of interest with $t \in \Upsilon$) respectively written in a Lagrangian description as (Malvern 1969):

$$\rho J = \rho_0 \tag{1}$$

$$\nabla \cdot \boldsymbol{\sigma} + \rho \boldsymbol{b}_f = \rho \ddot{\boldsymbol{u}} \tag{2}$$

$$-\rho c \dot{T} - \nabla \cdot \boldsymbol{q} + \rho r - T\boldsymbol{\beta}{:}\boldsymbol{d} + \rho r_{\text{int}} = 0 \tag{3}$$

$$-\boldsymbol{q} \cdot \nabla T + D_{\text{int}} \geq 0 \tag{4}$$

together with appropriate boundary and initial conditions and adequate constitutive relations for the Cauchy stress tensor $\boldsymbol{\sigma}$ (which is symmetric for the non polar case adopted in this work), the tangent

specific heat capacity c, the heat flux vector $\boldsymbol{q}$, the tangent conjugate of the thermal dilatation tensor $\boldsymbol{\beta}$, the specific internal heat source r_{int} and the internal dissipation D_{int}. In these equations, ∇ is the spatial gradient operator, the superposed dot indicates time derivative and the subscript 0 applied to a variable denotes its value at the initial configuration Ω_0. Moreover, ρ is the density, $\boldsymbol{u}$ is the displacement vector, J is the determinant of the deformation gradient tensor $\boldsymbol{F}$ ($\boldsymbol{F}^{-1} = \boldsymbol{1} - \nabla \times \boldsymbol{u}$, with $\boldsymbol{1}$ being the unity tensor), $\boldsymbol{b}_f$ is the specific body force vector, T is the temperature, r is the specific heat source and $\boldsymbol{d}$ is the rate-of-deformation tensor ($\boldsymbol{d} = 1/2(\nabla \times \boldsymbol{v} + \boldsymbol{v} \times \nabla)$, where $\boldsymbol{v} = \dot{\boldsymbol{u}}$ is the velocity vector). In this framework, a specific Helmholtz free energy function ψ, assumed to describe the material behaviour during the thermomechanical process, can be defined in terms of some thermodynamic state variables chosen in this work as the Almansi strain tensor $\boldsymbol{e}$ ($\boldsymbol{e} = 1/2(1 - \boldsymbol{F}^{-T} \cdot \boldsymbol{F}^{-1})$, where T is the transpose symbol), the temperature and a set of n_{int} phenomenological internal variables $\boldsymbol{\alpha}_k$ (usually governed by rate equations with $k = 1, ..., n_{\text{int}}$) accounting for the non-reversible effects (Celentano 2001). This free energy definition, based on the Doyle-Ericksen's approach (Doyle and Ericksen 1956), is only valid for small elastic strains and isotropic material response, both assumptions being normally accepted for metals and other materials. Invoking the Coleman's method (Coleman and Gurtin 1967), the following relationships are obtained:

$$\boldsymbol{\sigma} = \rho \frac{\partial \psi}{\partial \boldsymbol{e}}, \quad \eta = -\frac{\partial \psi}{\partial T},$$

is the specific entropy function,

$$c = -T\frac{\partial^2 \psi}{\partial T^2}, \quad \boldsymbol{\beta} = -\rho \frac{\partial^2 \psi}{\partial \boldsymbol{e}\,\partial T} = -\frac{\partial \boldsymbol{\sigma}}{\partial T}, \quad r_{\text{int}} = -\frac{1}{\rho_0}\left(T\frac{\partial \boldsymbol{q}_k}{\partial T} - \boldsymbol{q}_k\right)^{*}\frac{D\boldsymbol{\alpha}_k}{Dt}$$

and $D_{\text{int}} = \boldsymbol{q}_k^{*}\dfrac{D\boldsymbol{\alpha}_k}{Dt}$ where $\boldsymbol{q}_k = -\rho_0 \dfrac{\partial \psi}{\partial \boldsymbol{\alpha}_k}$ are the conjugate variables of $\boldsymbol{\alpha}_k$ and, acscording to the nature

of each internal variable, the symbols $*$ and $D(\cdot)/Dt$ appearing in the previous expressions respectively indicate an appropriate multiplication and a time derivative satisfying the principle of material frame-indifference (Malvern 1969). Furthermore, the heat flux vector at the spatial configuration is assumed to be given by the Fourier's law written as $\boldsymbol{q} = -k\nabla T$ where k is the conductivity coefficient. Additionally, a more restrictive dissipative assumption than that stated in Eq. (4) reads: $-\boldsymbol{q} \cdot \nabla T \geq 0$ and $D_{\text{int}} \geq 0$ (Malvern 1969). The first condition is automatically fulfilled for $k \geq 0$ while the second imposes restrictions over the constitutive model definition.

It is seen that the definitions of $\psi = \psi(\boldsymbol{e}, \boldsymbol{\alpha}_k, T)$ and $D\boldsymbol{\alpha}_k/Dt$ are crucial features of the formulation in order to derive the constitutive equations presented above.

The internal variables and their corresponding evolution equations are defined in this work within the associate rate-independent thermoplasticity theory context (Lubliner 1990, Simo 1995). A possible choice is given by the plastic Almansi strain tensor $\boldsymbol{e}^p$, the effective plastic deformation $\bar{\boldsymbol{e}}^{\,p}$ related to the isotropic strain hardening effect and the plastic yield entropy ζ^p (Celentano 2001). The consideration of ζ^p in this thermomechanical context is consistent with the principle of maximum plastic dissipation (Armero and Simo 1993, Celentano *et al.* 1999). The evolution equations for such plastic variables are written as:

$$L_v(\boldsymbol{e}^p) = \lambda \frac{\partial F}{\partial \tau} \qquad \dot{\bar{e}}^{\,p} = \lambda \qquad \dot{\zeta}^p = \lambda \frac{\partial F}{\partial T} \tag{5}$$

where $\boldsymbol{\tau}$ is the Kirchhoff stress tensor ($\boldsymbol{\tau} = J\boldsymbol{\sigma}$), L_v is the well-known Lee (frame-indifferent) derivative, λ is the plastic consistency parameter computed according to classical concepts of the plasticity theory (Simo 1995) and $F = F(\boldsymbol{\sigma}, \bar{e}^p, T)$ is the yield function governing the plastic behaviour of the solid such that no plastic evolutions occur when $F < 0$. A Von Mises yield function is adopted:

$$F = \sqrt{3J_2} - C^p \tag{6}$$

where J_2 is the second invariant of the deviatoric part of $\boldsymbol{\tau}$ and C^p is the plastic hardening function given by:

$$C^p = A^p(\bar{e}_0^p + \bar{e}^p)^{n^p} \tag{7}$$

where $\bar{e}_0^p$ is an assumed initial value of $\bar{e}^p$ such that $C^{th} = A^p \bar{e}_0^{p\,n^p}$ with C^{th} being the yield strength defining the material elastic bound. Moreover, A^p and n^p are hardening material parameters which, in general, can be temperature-dependent. Nevertheless, they are considered as constants in this work since the thermal softening effect has not been experimentally observed at the temperature levels developed during the tests described in Section 2 which allowed to derive such hardening parameters from the experimental-based correlation of the mean equivalent stress versus equivalent deformation curve. This last assumption leads to $\zeta^p = 0$. Furthermore, in this context the effective plastic deformation rate can be also computed as $\dot{\bar{e}}^p = \sqrt{2/3\boldsymbol{d}^p{:}\boldsymbol{d}^p}$, where $\boldsymbol{d}^p = L_v(\boldsymbol{e}^p)$ is the plastic rate-of-deformation tensor.

With these considerations, the following specific free energy function $\psi = \psi(\boldsymbol{e} - \boldsymbol{e}^p, \bar{e}^p, T)$ is proposed:

$$\psi = \frac{1}{2\rho_0}(\boldsymbol{e} - \boldsymbol{e}^p){:}\boldsymbol{C}^s{:}(\boldsymbol{e} - \boldsymbol{e}^p) - \frac{1}{\rho_0}(\boldsymbol{e} - \boldsymbol{e}^p){:}\boldsymbol{C}^s{:}\boldsymbol{e}^{th} + c^s[(T - T_{ref}) - T\ln(T/T_{ref})]$$

$$+ \frac{1}{\rho_0}(\boldsymbol{e} - \boldsymbol{e}^p){:}\boldsymbol{C}^s{:}\boldsymbol{\tau}_0 - \eta_0(T - T_0) + \psi_0 - \frac{1}{(n^p + 1)\rho_0}A^p(\bar{e}_0^p + \bar{e}^p)^{n^p + 1} + \frac{1}{\rho_0}C^{th}\bar{e}^p \tag{8}$$

where $\boldsymbol{C}^s$ is the secant isotropic elastic constitutive tensor, c^s is the secant specific heat capacity, T_{ref} is a reference temperature and $\boldsymbol{e}^{th}$ is the thermal Almansi strain tensor given by:

$$\boldsymbol{e}^{th} = \frac{1}{2}[1 - (1 - a_{th})^{2/3}]\boldsymbol{1} \tag{9}$$

where $a_{th} = \alpha_{th}^s(T - T_{ref}) - \alpha_{th0}^s(T_0 - T_{ref})$ with α_{th}^s being the secant volumetric thermal dilatation coefficient. Note that if $a_{th} \ll 1$, $\boldsymbol{e}^{th} = a_{th}/3\,\boldsymbol{1}$ which is, in fact, the classical expression for the infinitesimal thermal strain tensor.

Eq. (8) is a partially coupled form of defining ψ which considers the density at the initial configuration according to the simplification of the Doyle-Ericksen's approach (Doyle and Ericksen 1956). However, the elastic/plastic decomposition of ψ can be considered nowadays well established (see Lubliner 1990 and references therein) and it has extensively been used in different isothermal (Simo and Armero 1992, García Garino and Oliver 1993, Simo 1995, Goicolea *et al.* 1996) and

non-isothermal applications (Wriggers *et al.* 1989, Armero and Simo 1993, Simo 1995, Celentano *et al.* 1999, Celentano 2001). Moreover, as discussed by Celentano (2001), the additive decomposition of the Almansi strain tensor is recovered in this context through the multiplicative decomposition of the deformation gradient into elastic, thermal and plastic contributions. Besides, the superscript *s* denotes secant thermomechanical properties measured with respect to T_{ref}. Once more, by neglecting the temperature-dependency in the constant material parameters, the tangent variables respectively coincide with the secant ones (e.g., $c = c^s$) where, in addition, $T_{ref} = T_0$ is considered.

The stress-strain law (secant or hyperelastic form for the Cauchy stress tensor), the specific entropy function, the tangent conjugate of the thermal dilatation tensor, the specific internal heat source and the expression of the internal dissipation, all of them obtained from the above definition of ψ, are summarized in **Box 1**.

The tangent form of the stress-strain law commented above can be obtained applying standard procedures of the thermoplasticity theory (Simo 1995). Although this rate expression need not be calculated within the present hyperelastic context, its derivation is particularly relevant in the computation of the stiffness matrix appearing in the finite element formulation described in Section 4.

Finally, it is worth noting that the internal dissipation inequality is fulfilled owing to the adopted definition for the plastic rate equations.

4. Finite element formulation

The finite element equations derived from the proposed thermomechanical formulation presented above are briefly described in this Section together with some important features of the numerical strategy used to solve the resulting coupled system of discrete equations.

Following the standard procedures within the finite element framework (Zienkiewicz and Taylor 1989), the global discretized thermomechanical equations (equation of motion and energy balance, respectively) both including mass conservation can be written in matrix form for a certain time *t* as:

$$\boldsymbol{R}_U \equiv \boldsymbol{F}_U - \boldsymbol{M}\ddot{\boldsymbol{U}} - \boldsymbol{F}_\sigma = \boldsymbol{0}$$

$$\boldsymbol{R}_T \equiv \boldsymbol{F}_T - \boldsymbol{C}\dot{\boldsymbol{T}} - \boldsymbol{K}\boldsymbol{T} - \boldsymbol{L}_{\text{int}} - \boldsymbol{G}\dot{\boldsymbol{U}} = \boldsymbol{0} \tag{10}$$

where $\boldsymbol{R}_U$ and $\boldsymbol{R}_T$ are the so-called mechanical and thermal residual vectors, respectively. Moreover, $\boldsymbol{F}_U$ is the external force vector, $\boldsymbol{M}$ is the mass matrix, $\boldsymbol{U}$ is the nodal displacement vector, $\boldsymbol{F}_\sigma$ denotes the internal force vector, $\boldsymbol{F}_T$ is the external heat flux vector, $\boldsymbol{C}$ is the capacity matrix, $\boldsymbol{T}$ is the nodal temperature vector, $\boldsymbol{K}$ is the conductivity matrix, $\boldsymbol{L}_{\text{int}}$ is the internal heat source vector and $\boldsymbol{G}$ is the thermoelastic coupling matrix. The element expressions of these matrices and vectors are shown in **Box 2**. Note that $\boldsymbol{R}_U$ and $\boldsymbol{R}_T$ are respectively computed at the initial, using the well-known total Lagrangian approach (Crisfield 1991), and spatial configurations. In this context, all the variables involved in $\boldsymbol{R}_U$ need to be transformed to the initial configuration.

The integration of the terms containing time derivatives of $\boldsymbol{U}$ and $\boldsymbol{T}$ in system (10) is respectively carried out with the Newmark method and the generalized mid-point rule algorithm choosing the corresponding parameters that make both procedures unconditionally stable (Zienkiewicz and Taylor 1989). The last scheme has also been used to integrate the plastic rate equations presented above via

a return-mapping procedure (Crisfield 1991, Simo 1995).

   The numerical solution of system (10) is performed using a staggered scheme considering an improved isothermal split such that the displacement and temperature fields are respectively obtained by assuming isothermal conditions and a fixed elastic configuration for the mechanical and thermal residuals. The original infinitesimal strain algorithm proposed by Celentano *et al.* (1999) is extended in this work to account for large strains. This methodology shares some features of the adiabatic split developed by Armero and Simo (1993), such as its stability and preservation of the coupling degree of the thermomechanical formulation, with the additional advantage of solving the mechanical phase isothermally which is, in general, a simpler constraint to deal with than the isentropic condition of the adiabatic partition for the same phase. The jacobian matrices needed in the Newton-Raphson iterative process are shown in **Box 3**. Owing to the strong non-linearities inherent in the formulation, approximated expressions for J_{UU} and J_{TT} are considered for the iterative process, where K_U is the stiffness matrix, C_p is a coupling matrix due to plastic effects and C_{th} is the thermal coupling matrix. These matrices have been respectively derived from F_σ, L_{int} and $G\dot{U}$.

   In this total Lagrangian approach, the stiffness matrix consists of two terms usually called the material and geometric contributions respectively related to the elastoplastic constitutive behaviour and the non-linear effects of the adopted strain measure (Crisfield 1991).

   Although classical spatial interpolations for the displacement and temperature fields have been considered in system (10), an improved strain-displacement matrix $\overline{B}$, previously proposed by Celentano (2001) and checked in problems involving moderate deformations, is also employed in this work in order to overcome the volumetric locking effect on the numerical solution when incompressible plastic flows are studied. The performance of this methodology is now tested in a large strain situation like the necking process of a cylindrical tension specimen described below. Based on the deformation gradient standard decomposition into deviatoric and volumetric parts, and assuming a selective numerical integration for the volumetric part of F, the $\overline{B}$ matrix is obtained by linearization of the Green-Lagrange strain tensor. The expressions of this matrix for the 2D, axisymmetric and 3D cases can be found in the mentioned reference. It should mentioned that the $\overline{B}$ matrix has not a sparse structure. Nevertheless, the additional computations required at element level were found not to significantly increase the CPU times in comparison with the standard sparse strain-displacement matrix. This methodology is an alternative approach to the assumed strain mixed finite element method developed by Simo and Armero (1992) in which a sparse gradient operator is obtained with the drawback of computing and storing, at element level, enhanced strain parameters defined in such context. Note that these last operations are not needed in the present $\overline{B}$ algorithm and, hence, a simple computational implementation of it may be attained.

5. Numerical simulation and experimental validation

5.1 HE30 (BS 1474) aluminium alloy

   The necking process of a HE30 (BS 1474) aluminium alloy bar in an uniaxial tensile test has been extensively studied in recent years under isothermal conditions (see Goicolea *et al.* 1996). The objective of the present analysis is to validate the proposed formulation with available experimental and numerical results. The material properties are summarized in Table 4. The extensometer length

Table 4 Analysis of a HE30 (BS 1474) aluminium alloy cylindrical tension
specimen: material properties considered in the simulation

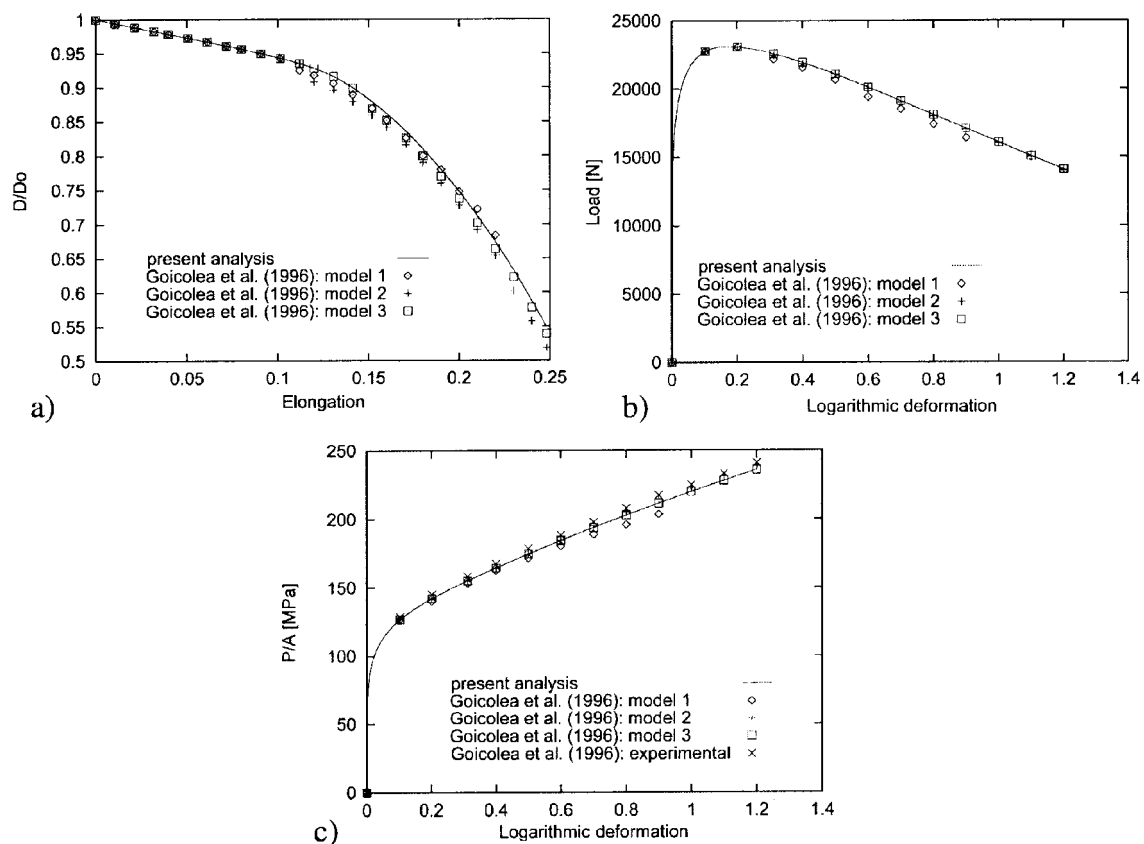|	
Young's modulus E	67000 MPa
Poisson's ratio v	0.3
Yield strength C^{th}	50.0 MPa
Hardening coefficient A^p	181.7 MPa
Hardening exponent n^p	0.159

Fig. 6 Analysis of a HE30 (BS 1474) aluminium alloy cylindrical tension specimen under isothermal conditions. Results at the section undergoing extreme necking: a) ratio of current to initial diameter versus axial elongation, b) load versus logarithmic deformation and c) mean true axial stress versus logarithmic deformation (model 1: hipoelastic explicit model, model 2: hipoelastic implicit model and model 3: hiperelastic implicit model; see Goicolea *et al.* 1996)

is 75 mm and the radius varies gradually from the extremes to the central (necking) zone from 8.1 mm to 7.95 mm. Due to the symmetry of the problem, only one quarter is considered in the computations. The finite element mesh used in the simulation is composed of nearly 400 axisymmetric four-noded isoparametric elements non-uniformily distributed (similar to that used in the cited reference)

including the $\overline{B}$ approach described above.

Fig. 6 shows the radii relation versus the elongation in the necking zone together with the load and mean true axial stress both against the logarithmic deformation. The numerical results obtained in this work are compared with other numerical predictions computed with very different formulations whose particular aspects are the stress-strain relationship, the time integration algorithm applied to the equation of motion, the return-mapping procedure to deal with the plastic evolution equations and the form to treat the plastic incompressibility (see Goicolea *et al.* 1996 for further details). Although the isothermal version of the present formulation shares some of these features (e.g., the implicit hiperelastic character), it should be emphasized that the proposed $\overline{B}$ approach is a distinctive contribution with respect to those developed in the already existing methodologies. An overall good agreement between the numerical results provided by the present analysis and those of the reference can be appreciated. Moreover, the numerical predictions fit very well the available experimental data for the $P/A - \varepsilon_p$ curve.

Table 5 presents a comparison between numerical results using the above mentioned models and experimental data for a logarithmic deformation of 0.90 in the necking zone. As can be seen, all the models give reasonably good responses which fall within the experimental uncertainty and, in particular, this is also the case for the results obtained with the formulation presented in this work.

Table 5 Analysis of a HE30 (BS 1474) aluminium alloy cylindrical tension specimen: comparison between numerical and experimental results for $\varepsilon_p = 0.90$ in the necking zone

Analysis type	P/A [MPa]	P [kN]
Present analysis	211.5	17.1
Goicolea *et al.* (1996): hipoelastic explicit model	207.0	16.8
Goicolea *et al.* (1996): hipoelastic implicit model	217.0	17.5
Goicolea *et al.* (1996): hiperelastic implicit model	215.0	17.3
Goicolea *et al.* (1996): experimental	213±15	17.2±1.2

Table 6 Analysis of a SAE1020 cylindrical tension specimen: material properties considered in the simulation

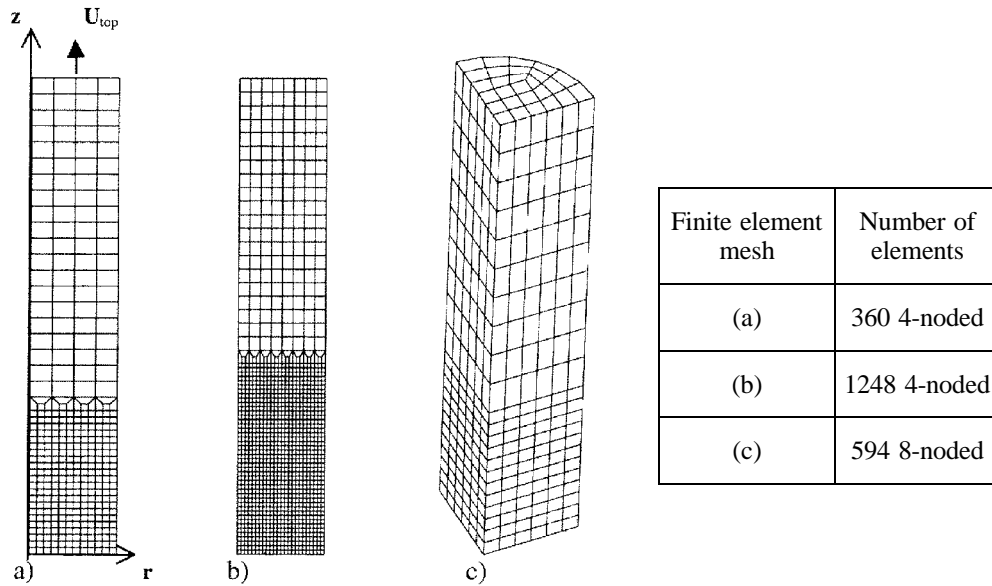|	
Young's modulus E	222054 MPa
Poisson's ratio ν	0.3
Thermal dilatation coefficient (secant) α_{th}^s	1.0×10^{-5} 1/°C
Yield strength C^{th}	333.0 MPa
Hardening coefficient A^p	730.75 MPa
Hardening exponent n^p	0.1845
Density (initial) ρ_0	7800 kg/m^3
Specific heat (secant) c^s	460 J/kg°C
Conductivity k	45 J/ms°C
Heat transfer coefficient (edge of specimen-air) h	60 J/m^{2}s°C
Heat transfer coefficient (top boundary-upper part of specimen) h	1000 J/m^{2}s°C

Fig. 7 Analysis of a SAE1020 steel cylindrical tension specimen: finite element meshes used in the analysis

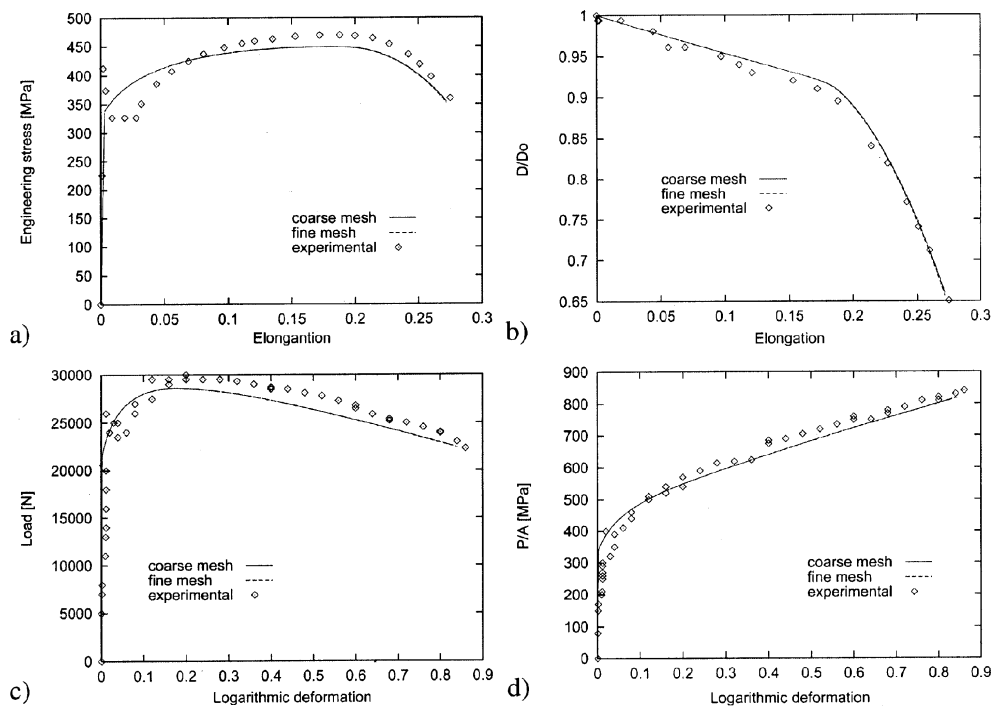| Finite element mesh	Number of elements
(a)	360 4-noded
(b)	1248 4-noded
(c)	594 8-noded

Fig. 8 Analysis of a SAE1020 steel cylindrical tension specimen under nearly isothermal conditions. a) Engineering stress-strain relationship (average experimental values). Results at the section undergoing extreme necking: b) ratio of current to initial diameter versus axial elongation, c) load versus logarithmic deformation and d) mean true axial stress versus logarithmic deformation

5.2 SAE1020 steel

The finite element thermomechanical formulation presented above is used to simulate the material behaviour during the tensile tests described in Section 2. The material properties of the SAE1020 mild steel considered in the numerical analysis are shown in Table 6. Different spatially non-uniform discretizations composed of isoparametric finite elements have been chosen in order to assess the mesh sensitivity for the large strains expected in the necking zone. A fourth and an eighth of the specimen are respectively discretized for the 2D axisymmetric and 3D cases with a height of 25 mm (half of the initial extensometer length) and a linear radius variation along the bar according to the geometry specifications depicted in Fig. 1. The details of the three meshes considered in the computations are presented in Fig. 7 where U_{top} denotes the axial displacement imposed at the top boundary assuming a rate of 2.5 mm/min up to a value of 6.8 mm which corresponds to a fracture elongation of 27.2% (see Table 2). Heat transfer conditions to the surrounding environment (at 20ºC) and to the upper part of the specimen are also considered (see Table 6). The high value of the heat transfer coefficient at the top boundary has been estimated according to an assumed outward heat flux to the upper part of the specimen. However, as previously mentioned, no relevant temperature rise is developed due to the low load cell speed considered in this first nearly isothermal analysis. Moreover, the analysis is performed with $b_f = 0$ and $r = 0$.

The engineering stress-strain relationship and some results at the section undergoing extreme necking can be all found in Fig. 8. In particular, the ratio of current to initial diameter in terms of the elongation plotted for both 2D meshes starts with a linear relationship, reflecting uniform distributions of stresses and strains, which presents an approximate slope of 0.5 due to the incompressibility nature of the plastic flow. The same situation is kept up to an elongation of 18%. Afterwards, a sudden reduction of the diameter takes place causing the necking formation and, hence, non-homogeneous stress and strain distributions along the specimen. As can be seen, both discretizations are able to properly describe such phenomenon as their predictions practically overlap. This fact is also repeated in the results presented below. The simulated diameter ratio at the fracture stage is 0.66 which agrees very well with the experimental value 0.65 derived from the dimensions shown in Fig. 3. Numerical and experimental results corresponding to the load versus logarithmic deformation curve are also plotted where an overall good agreement between such results can be observed. The major discrepancies are found at the beginning of the test, where the plastic deformation without hardening occurs, owing to the hardening parameters derived from the correlation of Fig. 4 do not adequately capture the material behaviour at this stage. At the point of maximum load, note that the well-known simplified relationship (Nádai 1950, Bridgman 1952), stating that the related deformation has to be equal to the hardening exponent, is approximately verified (see Table 2). Moreover, numerical predictions of the engineering stress-strain relationship and the mean true axial stress as a function of the logarithmic deformation are presented together with the respective experimentally measured values for comparison. Once more, the simulation reasonably adjusts the experimental data. The larger differences between the experimental and predicted results are due to the same reasons already commented for the load-logarithmic deformation curve. The big amount of plastic hardening can clearly be appreciated. Although the load decreases from a logarithmic deformation of 18% onwards, it should be noted that the mean true axial stress increases up to the fracture stage. This fact means that a geometrical instability occurs (instead of a constitutive instability) since, as already commented in Section 2, the effect on the stress caused by the reduction of the transversal area at the necking zone predominates over the
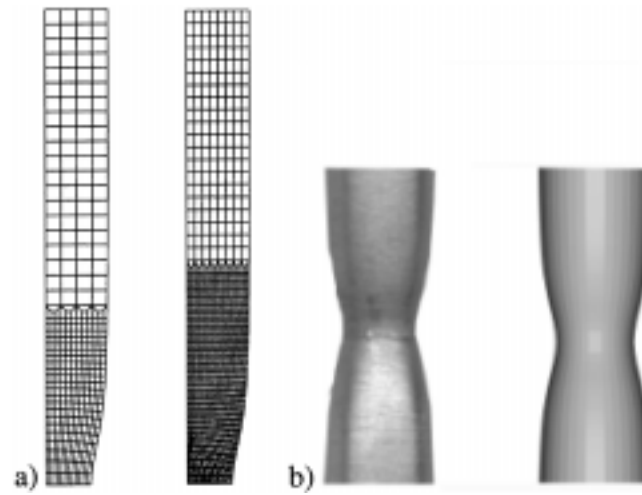
Fig. 9 Analysis of a SAE1020 steel cylindrical tension specimen under nearly isothermal conditions. Results at the end of the analysis corresponding to the fracture stage for an elongation of 27.2%: a) deformed 2D meshes and b) necking zone (left: experimental and right: simulation)
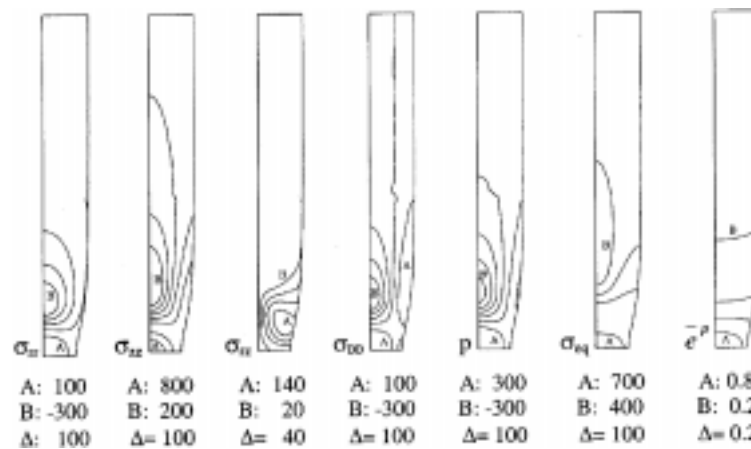

Fig. 10 Analysis of a SAE1020 steel cylindrical tension specimen under nearly isothermal conditions: stress (in MPa) and effective plastic deformation contours at the end of the analysis corresponding to the fracture stage for an elongation of 27.2%

material hardening. At this level of deformation, the regions of the specimen outside the necking zone are being elastically unloaded.

The deformed coarse and fine 2D meshes at the fracture elongation are shown in Fig. 9. A good qualitative comparison of the geometric configuration at the necking zone between the simulation and the broken specimen is also presented.

Stress and effective plastic deformation contours at the end of the analysis can be found in Fig. 10
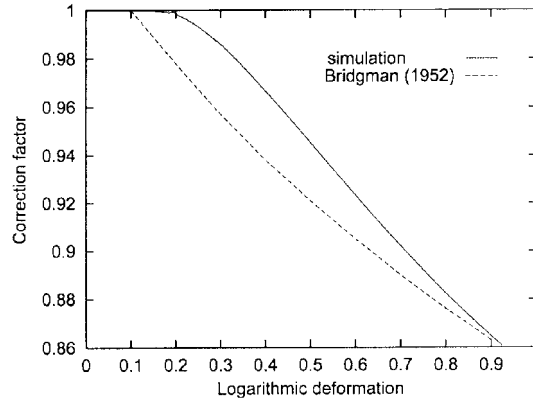
Fig. 11 Analysis of a SAE1020 steel cylindrical tension specimen: correction factor for the stress distribution
at the neck

Table 7 Analysis of a SAE1020 cylindrical tension specimen: comparison of results at the
fracture elongation under nearly isothermal conditions

Finite element mesh	D/Do	Load [N]	P/A [MPa]
2D 4-noded (coarse mesh)	0.66	22526	814
2D 4-noded (fine mesh)	0.66	22360	817
2D 8-noded (coarse mesh)	0.65	22229	820
2D 4-noded without $\overline{B}$ (coarse mesh)	0.82	27623	649
3D 8-noded	0.67	22989	787
3D 8-noded without $\overline{B}$	0.88	27991	560

including the radial, axial, shear and hoop components of $\boldsymbol{\sigma}$ together with the pressure $p = 1/3 \, \mathrm{tr}(\boldsymbol{\sigma})$
(tr is the trace symbol) and the equivalent stress σ_{eq} given by $\sqrt{3J_2}$. Non-uniform distributions are
clearly obtained due to the complex deformation pattern of the neck. Remarkably, a compressive
pressure state occurs at the center of the bar. This fact has also been pointed out by Armero and
Simo (1993) and Goicolea *et al.* (1996) in the tension analysis of other materials. As expected, the
maximum values of σ_{eq} and consequently of $\overline{e}^p$ are concentrated in the neck. Note that values
around 0.20 of effective plastic deformation mainly found at the rear part of the specimen indicate
the level of uniform deformation experienced until the maximum load is reached (see Fig. 8).
Furthermore, some assumptions considered in the analytical study of Bridgman (1952) at the neck
are ratified by the simulation, e.g., σ_{eq} and $\overline{e}^p$ are approximately constant, σ_{rr} and $\sigma_{\theta\theta}$ present a
strong variation but the condition $\sigma_{rr} \approx \sigma_{\theta\theta}$ is fullfiled, $\sigma_{zz} \approx \sigma_{eq} + \sigma_{rr} > \sigma_{eq}$ that explains the need to
correct the stress distribution (see Table 3), $p \approx \sigma_{eq}/3 + \sigma_{rr}$, $e_{zz} \approx -2e_{rr}$ up to the maximum load and
$e_{rr} \approx e_{\theta\theta}$ during the whole test.

Although the specimen fracture can not be predicted by the formulation described in Section 3,
the obtained numerical predictions correctly describe the experimental observations during the
tension process.

Fig. 11 compares the correction factor of Table 3 proposed by Bridgman (1952) with that
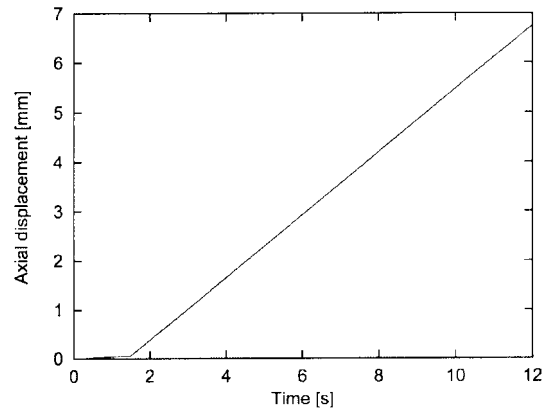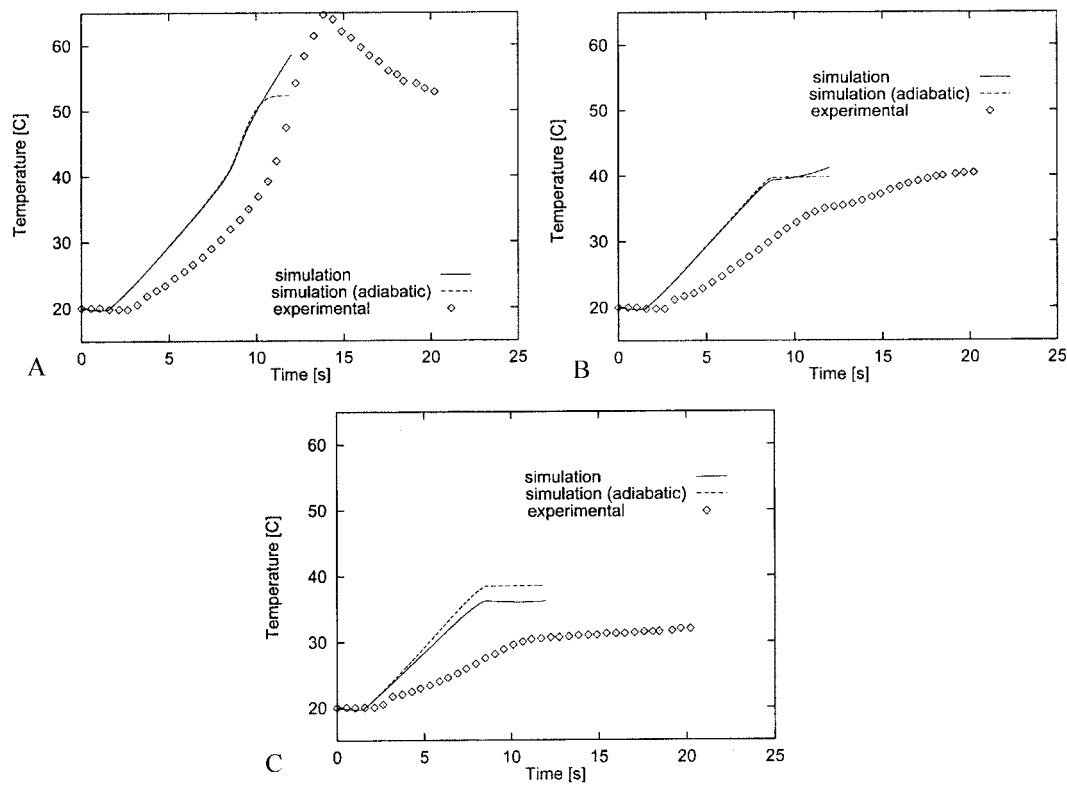
Fig. 12 Analysis of a SAE1020 steel cylindrical tension specimen: history of the imposed axial displacement at the top boundary considered in the thermomechanical non-isothermal analysis

Point positions at the initial configuration	A	B	C
Radial direction [mm]	4.5	4.5	4.5
Axial direction [mm]	5.0	15.0	25.0

Fig. 13 Analysis of a SAE1020 steel cylindrical tension specimen under non-isothermal conditions: temperature evolutions at points A, B and C of the specimen

predicted by the simulation as the quotient between the average equivalent stress at the neck and the mean true axial stress *P/A*. It can be seen that these curves present different ranges of deformation with uniform stress distribution where, in agreement with the remarks commented above, the simulated correction factor is relevant for deformations larger than 0.2. The maximum discrepancy in both correction factors is, however, less than 2%.

A numerical assessment of different discretizations and element topologies is illustrated in Table 7. A 2D 8-noded mesh, simply obtained by adding the mid-side nodes to the 2D 4-noded coarse mesh, is included since it has been long recognized that its higher order interpolation is adequate to deal with large strain plasticity models and, for this reason, the corresponding results are usually taken as reference numerical solutions in this kind of applications. However, the main drawback of such discretization is its usually large computational cost in comparison with those of 2D 4-noded meshes for a similar accuracy in the numerical predictions. The results without using the $\overline{B}$ technique briefly described in Section 4 are also considered which, as expected, reveal an excessive stiff response since they do not include any particular numerical treatment of the plastic incompressibility. On the contrary, very good predictions are found for the 2D and 3D cases
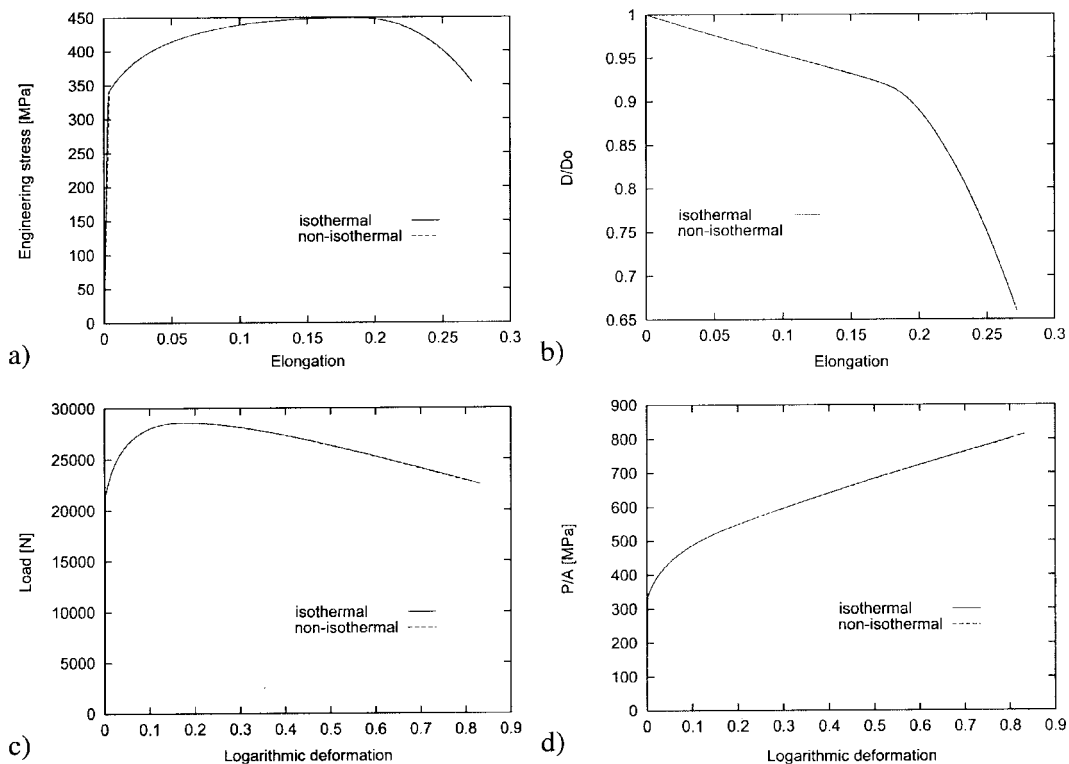

Fig. 14 Analysis of a SAE1020 steel cylindrical tension specimen under nearly isothermal and non-isothermal conditions. a) Engineering stress-strain relationship. Results at the section undergoing extreme necking: b) ratio of current to initial diameter versus axial elongation, c) load versus logarithmic deformation and d) mean true axial stress versus logarithmic deformation

including the $\overline{B}$ approach which, in addition, compare satisfactorily with the 2D 8-noded solution and, as commented above, with the experimental data.

In order to be able to observe significant temperature increments in the specimen during the test, a second analysis is performed considering a load cell speed of 100 mm/min which is expected to generate non-isothermal conditions characterized by higher plastic work rates transformed into heat.

It is a well-known experimental fact that the elongation rate existing at the extensometer length is in general different from the load cell speed during the tension process. With the aim of properly simulating the test under realistic conditions, an adequate history of the imposed axial displacement at the top of the boundary has to be taken into account in the simulation. At the beginning of the test, i.e., during the elastic deformation, a very low strain rate is observed. Then, the elongation rate gradually tends to the nominal load cell velocity reaching the nominal speed value only once the neck formation starts. For simplicity, however, a piecewise linear interpolation of the axial displacement considered in the thermomechanical non-isothermal analysis is depicted in Fig. 12.

The coarse 2D 4-noded mesh (see Fig. 7) with a time step of 0.01 s have been employed in the computations.

Numerical and experimental temperature evolutions at the thermocouple locations described in Section 2 are plotted in Fig. 13. According to the axial displacement history imposed at the top boundary (see Fig. 12), the temperature remains almost constant at the beginning of the test and then starts increasing uniformly along the specimen due to the homogeneous distribution of the plastic strain occurring up to the neck formation. Once the necking takes place (at approximately 11 s and 9 s for the experimental and numerical results, respectively), different temperature evolutions are obtained for such thermocouple locations: the temperature at point A suddenly increases owing to the concentrated heating generated by plastic deformation in the necking zone while, on the other hand, a decreasing temperature rate is observed for points B and C as a consequence of the elastic unloading experienced by them. Although the numerical predictions do not quantitatively match the experimental data, it should be noted that a reasonably good qualitative physical description of the thermal phenomenon is attained since the simulated temperature trends fit those obtained in the laboratory. The main reason of such discrepancy may be attributable to the time delay in the thermocouple measurements (estimated in 2 s) which, as commented in Section 2, is apparent in the experimental curves. Other possible sources leading to explain the differences between the experimental and numerical results are: 1) the simplified curve adopted for the history of the imposed axial displacement at the top boundary (see Fig. 12) which provides larger strain rates (and hence higher temperatures) than those existing in the experiments and 2) the difficulties associated with the temperature measurements due to the movement experienced by the thermocouples during the deformation process that make the numerical-experimental comparison hard since small indeterminations in the geometric location of such measurement points may give large errors due to the high temperature gradients present in the specimen.

Table 8 Analysis of a SAE1020 cylindrical tension specimen: comparison of results at the fracture elongation for different analyses using the 2D 4-noded coarse mesh

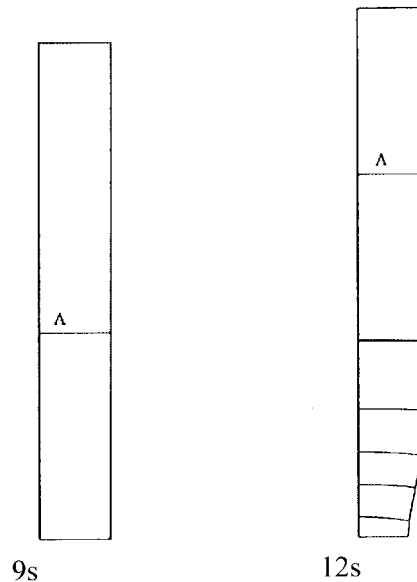| Analysis type	*D/Do*	Load [N]	*P/A* [MPa]
Isothermal	0.66	22526	814
Non-isothermal	0.67	22839	801

Fig. 15 Analysis of a SAE1020 steel cylindrical tension specimen under non-isothermal conditions: temperature contours at different times of the analysis. Isotherms are 10°C apart where line "A" corresponds to 40°C.

An additional foreseeable fact confirmed by the simulation is the nearly adiabatic conditions (corresponding to $k = 0$ and $h = 0$) existing during the test since a negligible amount of heat is transferred to the environment (see Fig. 13). Moreover, as in the nearly isothermal problem, it should be mentioned that the inertia effects does not play any significant role in this case.

Similar results to those presented in Fig. 8 are now plotted in Fig. 14 for non-isothermal conditions. As can be seen, the mechanical material response is not practically affected by thermal deformation during the tension process for the specified elongation rate. This also agrees with the experimental observations. A summary of these results can be found in Table 8.

Finally, Fig. 15 shows numerical temperature contours at two different times of the analysis corresponding to uniform and non-uniform heat generation stages, respectively. Once again, high temperature and temperature gradients in the necking zone can clearly be seen when the specimen fracture occurs.

6. Conclusions

Experimental and numerical analyses of the thermomechanical behaviour occurring in SAE1020 mild steel cylindrical specimens during the standard tensile test have been presented. A characterization of the material response has been firstly carried out in order to obtain the stress-strain curve, the diameter evolution at the neck and the history of temperatures caused by plastic deformation. From these data, elastic and hardening parameters have been derived applying a well established methodology. Moreover, a finite element large strain thermoelastoplasticity-based

formulation has been proposed and used to simulate the tensile deformation process. Some original features of such formulation have also been discussed.

This approach has been preliminarily validated with existing experimental and numerical results for an isothermal case considering HE30 (BS 1474) specimens. Afterwards, as mentioned above, it has applied to study the thermomechanical behaviour of SAE1020 steel during the test.

From the analysis of such thermomechanical process, several comments may be drawn. The low and high load cell speeds considered in the study have respectively led to nearly isothermal and non-isothermal conditions due to the different strain rates achieved in the specimen. Nevertheless, the mechanical behaviour for such cases was found to be practically independent of thermal and strain rate effects. The numerical results obtained with the proposed formulation have been satisfactorily validated with the experimental measurements related to the mechanical response. In particular, the diameter of the neck at the fracture stage and the load history during the test have been very well predicted by the simulation. Although some discrepancies between the numerical and experimental temperature evolution have been observed, the overall trends have been properly captured by the model. Finally, a good performance of the approach designed to preclude the volumetric locking effect on the numerical solution for incompressible plastic flows has been attained.

Acknowledgements

References

Annual Book of ASTM Standards (1988), Section 3: Metals Test Methods and Analytical Procedures.
Armero, F. and Simo, J. (1993), "A priori stability estimates and unconditionally stable product formula algorithms for non-linear coupled thermoplasticity", *Int. J. Plasticity*, **9**, 149-182.
Bridgman, P. (1952), *Studies in Large Plastic and Fracture*, McGraw-Hill Book Company, London.
Celentano, D., Gunasegaram D. and Nguyen T. (1999), "A thermomechanical model for the analysis of light alloy solidification in a composite mould", *Int. J. Solids and Struct.*, **36**, 2341-2378.
Celentano, D. (2001), "A large strain thermoviscoplastic formulation for solidification of S.G. cast iron in a green sand mould", *Int. J. Plasticity*, **17**, 1623-1658.
Coleman, B. and Gurtin, M. (1967), "Thermodynamics with internal state variables", *J. Chem. Phys.*, **47**(2), 597-613.
Crisfield, M. (1991), *Non-linear Finite Element Analysis of Solids and Structures*, **1-2**. John Wiley & Sons, Chichester.
Dieter, G. (1988), *Mechanical Metallurgy - SI Metric Edition*, McGraw-Hill Book Company, London.
Doyle, T. and Ericksen, J. (1956), "Nonlinear elasticity", *Adv. Appl. Mech.*, **4**.
García Garino, C. and Oliver, J. (1993), "A numerical model for elastoplastic large strain problems", Fundamentals and applications, *Proc. COMPLAS III*, 117.

Goicolea, J., Gabaldón, F. and García Garino, C. (1996), "Analysis of the tensile test using hypo and hyperlastic models (in Spanish)", *Proc. III Congress on Numerical Methods in Engineering*, 875-885.
Lubliner, J. (1990), *Plasticity Theory*, Macmillan Publishing.
Malvern, L. (1969), *Introduction to the Mechanics of a Continuous Medium*, Prentice-Hall, Englewood Cliffs.
Nádai, A. (1950), *Theory of Flow and Fracture of Solids*, McGraw-Hill Book Company, London.
Simo, J. and Armero, F. (1992), "Geometrically non-linear enhanced strain mixed methods and the method of incompatible modes", *Int. J. Numer. Meth. Eng.*, **33**, 1413-1449.
Simo, J. (1995), *Topics on the Numerical Analysis and Simulation of Plasticity*, Handbook of Numerical Analysis, Vol. III, Elsevier Science Publishers.
Wriggers, P., Miehe, C., Kleiber, M. and Simo, J. (1989), "On the coupled thermo-mechanical treatment of necking problems via finite-element-method", *Proc. COMPLAS II*, 527-542.
Zerilli, F. and Armstrong, W. (1987), "Dislocation-mechanics-based constitutive relations for material dynamics calculations", *J. Appl. Phys.*, **61**(5), 1816-1825.
Zienkiewicz, O. and Taylor, R. (1989), *The Finite Element Method*, 4th Edition, **1-2**. McGraw-Hill, London.

BOX 1

Variables of the constitutive model

- Secant stress-strain law (Cauchy stress tensor):

$$\boldsymbol{\sigma} = \frac{1}{J}[\boldsymbol{C}^s{:}(\boldsymbol{e} - \boldsymbol{e}^p - \boldsymbol{e}^{th}) + \boldsymbol{\tau}_0]$$

- Specific entropy function:

$$\eta = \frac{1}{\rho_0}(\boldsymbol{e} - \boldsymbol{e}^p){:}\boldsymbol{C}^s{:}e_T^{th}\boldsymbol{1} + c^s\ln(T/T_0) + \eta_0$$

where

$$e_T^{th} = \frac{1}{3}(1 - a_{th})^{-1/3}\alpha_{th}^s$$

- Tangent conjugate of the thermal dilatation tensor:

$$\boldsymbol{\beta} = \frac{1}{J}\boldsymbol{C}^s{:}e_T^{th}\boldsymbol{1}$$

- Specific internal heat source:

$$r_{\text{int}} = \frac{1}{\rho_0}[\boldsymbol{\tau}{:}L_v(\boldsymbol{e}^p) + (C^p - C^{th})\vec{e}^{\,p}]$$

- Internal dissipation:

$$D_{\text{int}} = [\boldsymbol{\tau}{:}L_v(\boldsymbol{e}^p) + (C^p - C^{th})\vec{e}^{\,p}]$$

BOX 2

Element matrices and vectors in the discretized thermomechanical equations

$$\boldsymbol{F}_U^{(e)} \,=\, \int_{\Omega_0^{(e)}} \boldsymbol{N}_U^T \boldsymbol{b}_{F_0} d\Omega_0 + \int_{\Gamma_{\sigma_0}^{(e)}} \boldsymbol{N}_U^T \bar{\boldsymbol{t}}_0 d\Gamma_{\sigma_0} + \sum_{j=1}^{n_{cU}} \boldsymbol{F}_{c_{Uj}}^{(e)}$$

$$\boldsymbol{M}^{(e)} \,=\, \int_{\Omega_0^{(e)}} \boldsymbol{N}_U^T \rho_0 \boldsymbol{N}_U d\Omega_0$$

$$\boldsymbol{F}_\sigma^{(e)} \,=\, \int_{\Omega_0^{(e)}} \overline{\boldsymbol{B}}^T S d\Omega_0$$

$$\boldsymbol{F}_T^{(e)} \,=\, \int_{\Omega^{(e)}} \boldsymbol{N}_T^T \rho r d\Omega + \int_{\Gamma_q} \boldsymbol{N}_T^T \overline{q}\, d\Gamma_q + \int_{\Gamma_q} \boldsymbol{N}_T^T h T_{env} d\Gamma_q + \sum_{j=1}^{n_{cT}} \boldsymbol{F}_{c_{Tj}}^{(e)}$$

$$\boldsymbol{C}^{(e)} \,=\, \int_{\Omega^{(e)}} \boldsymbol{N}_T^T \rho c \boldsymbol{N}_T d\Omega$$

$$\boldsymbol{K}^{(e)} \,=\, \int_{\Omega^{(e)}} (\boldsymbol{\nabla} \boldsymbol{N}_T)^T k \boldsymbol{\nabla} \boldsymbol{N}_T d\Omega + \int_{\Gamma_c^{(e)}} \boldsymbol{N}_T^T h \boldsymbol{N}_T d\Gamma_c$$

$$\boldsymbol{L}_{int}^{(e)} \,=\, \int_{\Omega^{(e)}} \boldsymbol{N}_T^T \rho r_{int} d\Omega$$

$$\boldsymbol{G}^{(e)} \,=\, \int_{\Omega^{(e)}} \boldsymbol{N}_T^T T \boldsymbol{\beta}^T \overline{\boldsymbol{B}}_L d\Omega$$

where

$\boldsymbol{N}_U$	: Shape function matrix for displacements.
$\boldsymbol{b}_{F_0}$	: Body force vector at initial configuration Ω_0.
$\bar{\boldsymbol{t}}_0$	: Traction vector at the boundary $\Gamma_{\sigma_0} \subset \Gamma_0$ ($\Gamma_0 = \partial\Omega_0$).
$\boldsymbol{F}_{c_U}^{(e)}$	: Point force vector at element (e) with n_{cU} loaded nodes.
$\overline{\boldsymbol{B}}$	: Strain-displacement matrix for large strains to avoid numerical locking due to incompressible plastic deformation. see Celentano (2001).
$S = J\boldsymbol{F}^{-1} \cdot \boldsymbol{\sigma} \cdot \boldsymbol{F}^{-T}$	: Second Piola-Kirchhoff stress tensor.
$\boldsymbol{N}_T$	: Shape function matrix for temperature.
$\overline{q}$	: Normal heat flux at the boundary $\Gamma_q \subset \Gamma$ ($\Gamma = \partial\Omega$).
h	: Heat transfer coefficient with a body and the environment at Γ_q.
T_{env}	: Environmental temperature.
$\boldsymbol{F}_{c_T}^{(e)}$	: Point heat flux vector at element (e) with n_{cT} loaded nodes.
$\overline{\boldsymbol{B}}_L$	: Rate-of-deformation-velocity matrix.
Superscript T	: transpose symbol.

BOX 3

Jacobian matrices for the improved isothermal split

$$\boldsymbol{J}_{UU} \,=\, -\frac{\partial \boldsymbol{R}_U}{\partial \boldsymbol{U}} \cong \boldsymbol{K}_U + \frac{4}{\Delta t^2} \boldsymbol{M}$$

$$\boldsymbol{J}_{TT} \,=\, -\frac{\partial \boldsymbol{R}_T}{\partial \boldsymbol{T}} \cong \boldsymbol{K} + \frac{1}{\Delta t}(\boldsymbol{C} - \boldsymbol{C}_p + \boldsymbol{C}_{th})$$

Element matrices appearing in the Jacobian expressions

$$\boldsymbol{K}_U^{(e)} = \int_{\Omega_0^{(e)}} \overline{\boldsymbol{B}}^T \frac{\partial \boldsymbol{S}}{\partial \boldsymbol{E}} \overline{\boldsymbol{B}} \, d\Omega_0 + \int_{\Omega_0^{(e)}} \overline{\boldsymbol{H}}^T S \overline{\boldsymbol{H}} \, d\Omega_0$$

$$\boldsymbol{C}_p^{(e)} = \int_{\Omega^{(e)}} N_T^T \rho \frac{\partial r_{\mathrm{int}}}{\partial T} N_T d\Omega$$

$$\boldsymbol{C}_{th}^{(e)} = \int_{\Omega^{(e)}} N_T^T T \boldsymbol{\beta}^T \frac{\partial \boldsymbol{d}^p}{\partial T} N_T d\Omega$$

where

Δt : Time increment.
$\partial \boldsymbol{S} / \partial \boldsymbol{E}$: Tangent elastoplastic constitutive tensor at initial configuration Ω_0 ($\boldsymbol{E}$: Green-Lagrange strain tensor).
$\overline{\boldsymbol{H}}$: Strain-displacement matrix for large strains derived by linearization of $\overline{\boldsymbol{B}}$.